Perovskite semiconductors for direct X-ray detection and imaging

Yirong Su[‡], Wenbo Ma[‡], and Yang (Michael) Yang[†]

State Key Laboratory of Modern Optical Instrumentation, College of Optical Science and Engineering, Zhejiang University, Hangzhou 310027, China

Abstract: Halide perovskites have emerged as the next generation of optoelectronic materials and their remarkable performances have been attractive in the fields of solar cells, light-emitting diodes, photodetectors, etc. In addition, halide perovskites have been reported as an attractive new class of X-ray direct detecting materials recently, owning to the strong X-ray stopping capacity, excellent carrier transport, high sensitivity, and cost-effective manufacturing. Meanwhile, perovskite based direct X-ray imagers have been successfully demonstrated as well. In this review article, we firstly introduced some fundamental principles of direct X-ray detection and imaging, and summarized the advances of perovskite materials for these purposes and finally put forward some needful and feasible directions.

Key words: halide perovskites; X-ray detection; optoelectronic materials

1. Introduction

X-ray possesses strong penetrating capacity, so has been widely applied to nondestructively probe the inside information of condensed matter subjects in various fields, e.g., industrial inspection, security check, medical examination, scientific research and so on[1−5]. Because of the difference in X-ray absorption efficiency among diverse matters, X-rays can carry the internal distribution information of subjects after penetrating them, then the corresponding images are obtained via the detection of these X-rays[6]. X-ray imaging is the visual form of X-ray detection, consisting of two main methods: planar imaging and computed tomography (CT)[7]. However, it is confirmed that high-dose X-ray will increase the risk of cancer to patient later in life due to the damaging of DNA by ionizing radiation, which leads to concern on personal safety, especially in medical applications[8]. The low performance and high cost of detection materials still severely limit the mass promotion of low-dose X-ray imaging, hence exploring new materials with superior properties for X-ray detection is quite necessary and urgently required.

Nowadays, two approaches are used to detect X-ray[9]. The dominant one is indirect detection using scintillators (such as CsI:Tl and Gd_2O_2S:Tb) to convert X-ray photons into low-energy photons (UV–visible-NIR) that could be detected by photodetectors. But for X-ray indirect imaging, the sensitivity and image quality are commonly mediocre due to lower conversion efficiency and the scattering induced optical crosstalk[10]. The other one is direct detection by X-ray photoconductors such as amorphous selenium (a-Se) which could realize high-resolution imaging in mammography[11]. Neverthe-less, the nearly-commercial a-Se direct X-ray imager has limited use because of its poor absorptivity of hard X-rays, low intrinsic X-ray sensitivity and insufficient charge transport ability. Therefore, the X-ray direct imaging is still developing on the way to mass marketing.

During the last decade, halide perovskites have emerged as a new generation of photoelectric materials and its remarkable performance has been attractive in the fields of solar cells, light-emitting diodes, lasers, photodetectors, etc.[12−15]. Halide perovskites have been also reported as a new class of X-ray direct detection materials in recent years, relying on their strong X-ray stopping power, high sensitivity, excellent carrier transport performance and low-cost solution processability[16−18]. Meanwhile, perovskite direct X-ray imagers have been successfully demonstrated as well[19−21].

This review will introduce the fundamental principle of direct X-ray detection and imaging, summarize the advances of perovskite materials for this purpose and finally put forward some needful and feasible directions in this field.

2. Mechanism of X-ray interacting with matter

X-rays are electromagnetic waves with wavelengths ranging from 0.01 to 10 nm (Fig. 1(a)). From a quantum mechanical perspective, a beam of X-rays can be quantized into photons of which the photon energy is tens of thousands of times greater than that of visible light. The intensity of X-rays is then given by the number of photons passing through a given area per unit time. There are two ways of interaction between X-ray photon and matter: scattering and absorption.

2.1. Scattering of X-ray

X-ray scattering can be divided into two types: Thomson scattering and Compton scattering. As shown in Fig. 1(b), Thomson scattering is elastic scattering of X-ray radiation by a free charged particle, which won't change the kinetic energy and frequency of X-ray photon. Thomson scattering is

Yirong Su and Wenbo Ma contributed equally to this work.
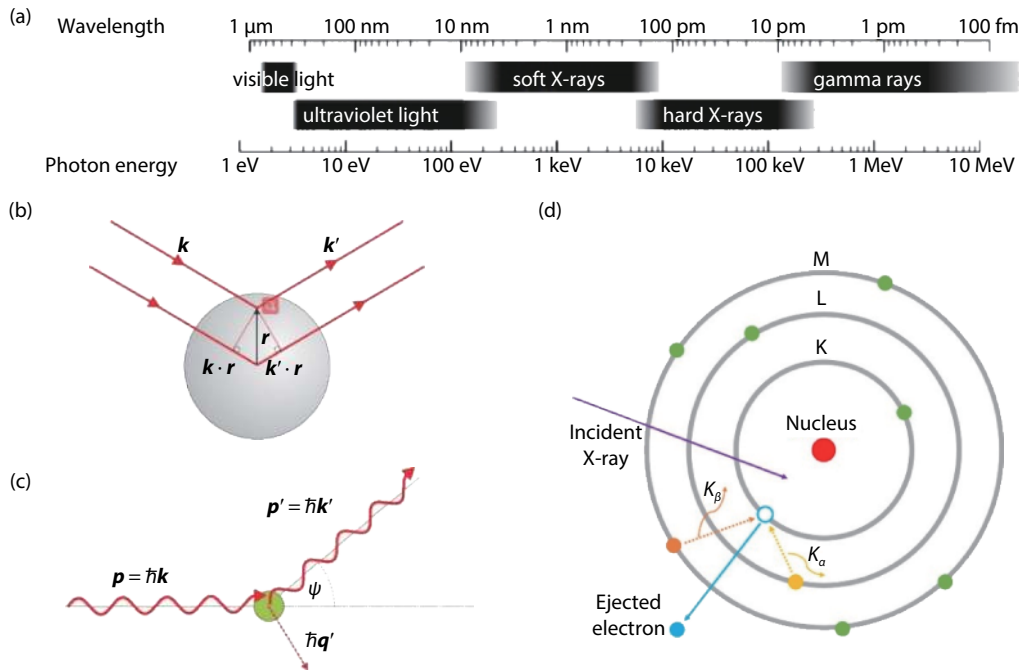Correspondence to: Y Yang, yangyang15@zju.edu.cn

Fig. 1. (Color online) (a) Spectrum region of X-ray to wavelength and photon energy. (b) Thomson scattering from an atom. An X-ray with a wave vector **k** scatters from an atom to the direction specified by **k′**. The scattering is assumed to be elastic. Reproduced with permission from Ref. [6]. (c) Compton scattering. A photon with energy $\varepsilon = \hbar c k$ and momentum $\hbar \mathbf{k}$ scatters from an electron at rest with energy mc^2. The electron recoils with a momentum $\hbar \mathbf{q}' = \hbar (\mathbf{k} - \mathbf{k}')$. Reproduced with permission from Ref. [6]. (d) Schematic diagram of photoelectric absorption process. An X-ray photon is absorbed and an electron ejected from the atom. The hole created in the inner shell (k) can be filled by Fluorescent X-ray emission. Electrons in an outer shell fill the hole, creating a photon. In this diagram the outer electron comes either from the L or M shell. In the former case the fluorescent radiation is referred to as the K_α line, and in the latter as K_β line.

also coherent and its coherence makes it exploited in investigations of the structure of materials. when Bragg's law is fulfilled, the X-ray will be elastic scattered from a crystal and coherently add up, then the scattering is restricted to lie at points on the reciprocal lattice. On the contrary, Compton scattering (Fig. 1(c)) is inelastic and incoherent scattering where the energy of incident X-ray photon may be transferred to the electron, resulting in lower frequency of scattered photon relative to that of incident one. The unique information on the electronic structure of materials could be obtained by Compton scattering. As the energy of incident X-ray photon is increased, the scattering becomes progressively more inelastic for a given scattering angle[6], in other words, the Compton scattering gradually dominates the X-ray scattering as the energy of incident photon increases.

2.2. Photoelectric absorption of X-ray

Fig. 1(d) illustrates the process of photoelectric absorption. After the incident X-ray photon is absorbed by an atom, the excess energy is transferred to an electron which will be ejected from the inner atom shell, creating a hole in that shell and leaving the atom ionized. The hole is subsequently filled by an electron from an outer shell with the simultaneous emission of a characteristic X-ray photon, of which the energy equals to the difference in the binding energies of electrons in these two shells. The characteristic emission X-ray is often used in X-ray fluorescence (XRF) analysis. By the way, the ionized atom could fill the hole in inner shell by expelling Auger electron as well.

The X-ray absorption can be quantitatively calculated by the following formula[6]:

$$\frac{I_0 - I(d)}{I_0} = 1 - e^{-\mu d} = 1 - e^{-\sigma \rho d},$$

where the I_0 and $I(d)$ are the X-ray intensities when the thicknesses are zero and d, μ is the linear absorption coefficient, d is the thickness, σ is the X-ray absorption cross-section and ρ is the density of matter. The absorption cross-section σ is a function of X-ray photon energy (ε) and atomic number (Z), approximatively exhibiting the following relationship:

$$\sigma \propto \frac{Z^4}{\varepsilon^3}.$$

It could be concluded that high energy X-ray has strong penetrating capability and the matter with heavy atoms is able to attenuate X-ray more efficiently. It is how the X-ray imaging is realized, and X-ray detection also puts forward some requirements to the detection materials for the same reason.

3. Direct X-ray detection and perovskite X-ray detectors

Direct detection is realized utilizing the ionization capacity of X-ray. When X-ray reaches a direct detector, the detecting materials are ionized, generating many free charges by the photoelectric effect and Compton scattering. In these two processes, the energy of X-ray photons is directly transferred to lots of charges, and then these excess charges are collected by electrodes under certain bias.

3.1. Ion chamber

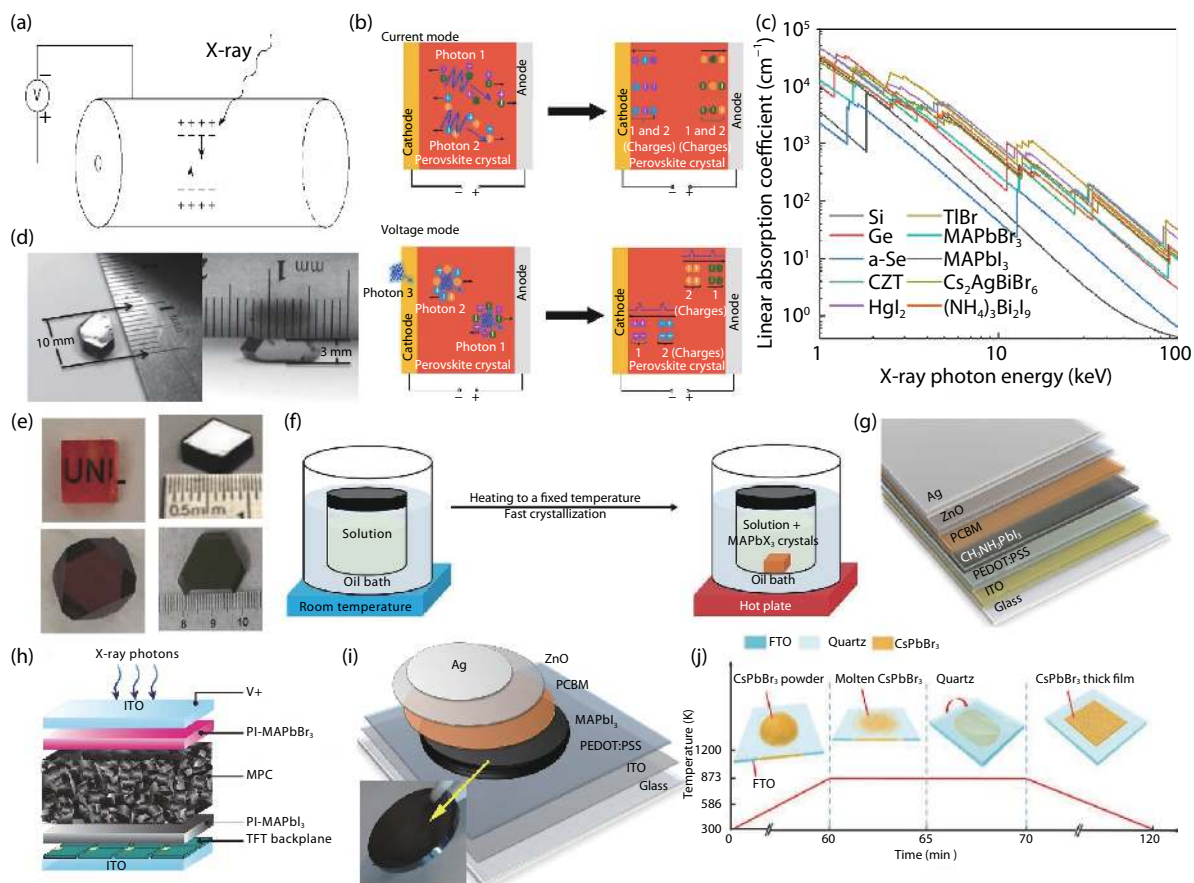The gas-filled detector worked at the voltage of ioniza-

Fig. 2. (Color online) (a) Working Principle of ion chamber. Reproduced with permission from Ref. [22]. (b) Semiconductor X-ray detectors' two types of work modes: current mode and voltage mode. Reproduced with permission from Ref. [23]. (c) The linear absorption coefficients of different kinds of perovskite and conventional X-ray detectors. (d) Images of a piece of MAPbI$_3$ single crystal. Reproduced with permission from Ref. [52]. (e) Images of perovskite single crystals of MAPbBr$_3$ (left top), c-MAPbI$_3$ (right top), Cs$_2$AgBiBr$_6$ (left bottom) and (NH$_4$)$_3$Bi$_2$I$_9$ (right bottom). Reproduced with permission from Ref. [16–18, 53]. (f) Schematic representation of the ITC apparatus in which the crystallization vial is immersed within a heating bath. The solution is heated from room temperature and kept at an elevated temperature (80 °C for MAPbBr$_3$ and 110 °C for MAPbI$_3$) to initiate the crystallization. Reproduced with permission from Ref. [54]. (g) Schematic of layer stacking of the MAPbI$_3$-based PIN photodiode. Reproduced with permission from Ref. [20]. (h) Illustration of an all-solution-processed digital X-ray detector. Reproduced with permission from Ref. [21]. (i) Device stack of the MAPbI$_3$-wafer-based X-ray detector. Inset: Free-standing MAPbI$_3$ wafer (thickness: 1 mm). Reproduced with permission from Ref. [55]. (j) Preparation scheme for a thick CsPbBr$_3$ film using the four-step hot-pressing method. Reproduced with permission from Ref. [56].

tion region (100 to 200 V), which is known as ion chamber[22] (Fig. 2(a)), is a type of common and inexpensive X-ray detector. A typical ion chamber instrument contains a chamber of about 200 cm³ filled with ambient air. When X-ray is absorbed by the air contained by the chamber, charge pairs (a positive ion and an electron) are produced, which are collected and amplified for recording the signal produced. However, on account of the slow detection speed, large volume, low X-ray attenuation and feeblish response, the application fields of ion chamber are severely restricted, not suitable for imaging and energy spectrum analysis.

3.2. Semiconductor X-ray detectors

3.2.1. Mechanism of semiconductor detectors

Direct X-ray semiconductor detector have become an attractive research field in recent years due to its good absorption, high sensitivity, fast response and excellent energy resolution[23]. Through the interaction of X-ray with semiconductor materials, electrons are excited from valence bands to high energy states, and then produce plenty of secondary elec-

trons. These high energy electrons are rapidly thermalized to conduction band minimum generating pairs of electrons and holes. A bias voltage is applied across the semiconductor which causes these charge carriers to move, leading to a signal. The energy needed to produce an electron–hole pair (EHP) in a semiconductor is typically about 2–10 eV, which is considerably less than that required to produce ionizations in air, therefore, a relatively large number of charge carriers is produced for each photon absorbed[22]. As depicted in Fig. 2(b), semiconductor X-ray detector has two types of work modes: current mode and voltage mode[23]. The former one is always used for dose rate measurement or generating imaging contrast[11], while the latter one is applied to photon counters or energy spectroscopy of X-ray[24].

3.2.2. Parameters of semiconductor detectors

The direct X-ray detection is generally considered to consist of three processes: absorption of X-ray energy, generation of carries (EHPs) and transport of charges[9]. There are several parameters in these processes influencing the performance of semiconductor X-ray detectors.

In the first process, the atomic number (Z) and density (ρ) of the detection material determine the linear absorption coefficient (μ), which represents the X-ray stopping power of this material at per unit thickness under certain photon energy. Fig 2(c) shows the linear absorption coefficients of different kinds of perovskites and some conventional X-ray detecting materials. In order to maximize X-ray energy utilization and reduce the risk of radiation leakage, semiconductor layer needs sufficient thickness to completely absorb X-rays. However, larger thickness tends to cause undesirable problems. For example, it is difficult to fabricate large area thick film with high quality and the thick semiconductor has lower charge collection efficiency in most cases. Besides, a larger thickness can also damage the imaging quality of X-ray, because the lateral charge transport will cause signal crosstalk in the image read out circuit[25]. Hence, high Z and large ρ are essential for X-ray detection materials because they can decrease the X-ray absorption length.

In the carriers generation process, the EHP creation energy ($W_\pm$), which is defined as the amount of radiation energy required to create a single EHP, should be as small as possible because the free charge (ΔQ) generated from an absorbed radiation of energy (ΔE) could be calculated by the following formula[11]:

$$\Delta Q = \frac{e\Delta E}{W_\pm},$$

where e is the elementary charge. $W_\pm$ is proportional to the bandgap (E_g) in many material systems. It is well-known that $W_\pm \approx 3E_g$ for many crystalline semiconductors, which is so-called Klein rule[26, 27], so this means that the low E_g is beneficial to the carriers generation.

The transport and collection of carries is a pretty complicated process in semiconductor X-ray detector, and various of parameters are related. The central parameter is the product of carrier mobility and mean carrier lifetime ($\mu\tau$), which is normally called the range of the carrier. It represents the mean distance drifted by the carrier per unit electric field before the carrier disappears by recombination (or trapped by defects)[11]. Since X-ray detector has much thicker film thickness than the visible light detector, the $\mu\tau$ greatly limits the sensitivity of detector by influencing charge collection efficiency, where sensitivity is an important parameter to measure the performance of the detector. Materials with strong X-ray stopping capacity, lower $W_\pm$, high $\mu\tau$ product and high charge collection efficiency are needed to realize high-sensitivity devices. In same way, the larger electric field (bias voltage per unit thickness, F) applied on the X-ray detector can promote the output signal of X-ray detector as well, which improves the theoretical sensitivity during the detection process. When analyzing and comparing sensitivities, it is necessary to indicate the electric field applied across the device. But it doesn't mean that a large F is absolutely beneficial for X-ray detection because F can affect another important parameter, dark current (I_d). It affects the lowest detectable dose rate, in the unit of (μGy_{air}/s or nGy_{air}/s). The dark current should be as small as possible so as to obtain enough signal to noise ratio (SNR) and is normally attributed to two factors: injected carriers from contacts and intrinsic thermally activated carriers The former is mainly caused by the electrical filed F and the resistivity of

the material, while the latter is related to the E_g of semiconductor. In general, material with a broad bandgap likely has lower dark current, but the corresponding larger $W_\pm$ reduces the intrinsic X-ray sensitivity to some extent, which is quite paradoxical.

3.2.3. Development status of semiconductor X-ray detectors

Since Van Heerden first investigated silver chloride (AgCl) crystals as radiation detectors in 1945[28], semiconductor X-ray detectors have made much progress. Due to the excellent transport ability of charges, high-purity silicon (Si) and germanium (Ge) have been widely applied in X-ray (or γ-ray) spectrum measurement[22, 29–33]. Nevertheless, the narrow bandgaps of Si and Ge crystals cause considerable thermal noise, which need to be suppressed by ancillary cooling systems or bulky cryogenics resulting in inconvenience of application[31]. In addition, the weak X-ray absorption capacity (due to the lower Z) and poor radiation intolerance of them are also limiting the applied areas. In comparison to monoatomic semiconductors, compound semiconductors offer more possibilities for direct X-ray detection because of the tunable bandgap and introduction of high-Z elements. The cadmium zinc telluride ($Cd_{1-x}Zn_xTe$, $x < 0.2$, CZT) is typical case of compound semiconductors X-ray detectors[31, 32, 34]. Other semiconductor X-ray detectors have also realized fair performance based on HgI_2[35–39], PbI_2[37, 40, 41], PbO[25, 42], TlBr[43, 44] and so on.

3.2.4. Advantages of perovskite for semiconductor X-ray detectors

In recent years, halide perovskites (composition of ABX_3, X = Cl, Br or I) have revolutionized the development of compound semiconductor X-ray detectors due to many beneficial qualities of them. Firstly, each of common elements in halide perovskite material systems, e.g., Cs, Pb, Bi, Br and I, has a high Z, meaning a strong stopping power and a favorable absorption efficiency. Meanwhile, narrower bandgaps of halide perovskites give rise to smaller $W_\pm$, which produce high intrinsic X-ray sensitivity. Furthermore, perovskites own outstanding charge transportation ability (long carrier lifetime and low trap density), leading to their $\mu\tau$ products much better than that of conventional compound semiconductor X-ray detectors[45]. Table 1 summarizes the various parameters of part of conventional and most of perovskites X-ray direct detectors in researches through the years.

In addition to their superior performances, solution-processed perovskites have another significant advantage, i.e. the low cost both in raw materials and manufacturing techniques[46, 47], which provides more chance for cosmically commercialization of perovskite X-ray detectors. Perovskites also surprisingly perform well in radiation tolerance and self-healing[48, 49], which is explained by the defect tolerance (or defect relaxation)[23, 50, 51].

3.3. Development progress of perovskite X-ray detectors

3.3.1. Advance in perovskite single crystal X-ray detectors

Single crystal is quite infrequent in the past compound semiconductor X-ray detectors, because the single crystal growth process of other materials is often expensive and

Table 1. Performances and parameters of part of conventional and perovskite X-ray direct detectors. In "status" column, A is amorphous, S is single-crystal and P is polycrystalline.

Material	Linear absorption coefficients to 50 keV (cm⁻¹)	$W_\pm$ (eV)	$\mu\tau$ (cm² V⁻¹)		F (V/cm)	Sensitivity ($\mu C/(Gy\cdot cm^2)$)	Lowest detectable dose rate (nGy$_{air}$/s)	Status (A, P or S)	Ref.
			$\mu_e\tau_e$	$\mu_h\tau_h$					
Si	1.022	3.62	>1	~ 1	0.5	8	<8300	S	[30–32, 71]
CZT	60.63	~ 4.6	$10^{-3} – 10^{-2}$	10^{-5}	0.1–1	318	50	S	[32, 34, 72, 73]
a-Se	3.864	45	$3 \times 10^{-7}–10^{-5}$	$10^{-6}–6 \times 10^{-5}$	>10⁴	20	–	A	[11, 21, 57]
MAPbBr₃	19.41	6.03	1.2×10^{-2}		0.5	80	500	S	[16]
MAPbBr₃(Si)	19.41	6.03	1.39×10^{-4}		~ 35	2.1×10^4	<100	S	[19]
MAPbBr₃(PIN)	19.41	6.03	—		150	2.36×10^4	–	S	[59]
MAPbI₃(Cuboid)	40.61	~ 4.4	1.1×10^{-4}		10	968.9	–	S	[53]
MAPbI₃(GA alloyed)	<40.61	~ 4.5	1.25×10^{-2}		~ 42	2.3×10^4	16.9	S	[60]
CsPbBr₃(QDs)	35.07	~ 5.9	—		1000	1450	–	S	[62]
CsPbBr₃(Rb doped)	35.07	~ 5.9	7.2×10^{-4}		~ 200	8.1×10^3	–	S	[63]
CsPbI₃(1D)	57.06	~ 6.8	3.63×10^{-3}		41.7	2.37×10^3	219	S	[64]
Cs₂AgBiBr₆	39.08	5.61	1.21×10^{-3}, 6.3×10^{-3}, 5.51×10^{-3}, 1.94×10^{-3}, —, 5.95×10^{-3}		33, 250, 5000, 227, 500, 500	4.2, 105, 250, 288.8, 988,1974	–	S/P	[17, 18, 63, 66–68]
(NH₄)₃Bi₂I₉	46.98	5.47	1.1×10^{-2}//, 4×10^{-3}⊥		50	8.2×10^3//, 803⊥	55	S	[18]
(DMEDA)BiI₅	~ 40	5.15	—		4940	72.5	–	S	[69]
MAPbI₃(PV)	40.61	~ 4.4	2×10^{-7}		~ 8000	1.75	–	P	[20]
MAPbI₃(Flat detector)	40.61	~ 4.4	1×10^{-4}		~ 2410	3.8×10^3	–	P	[21]
MAPbI₃(Wafer)	40.61	~ 4.4	2×10^{-4}		5700	2.527×10^3	–	P	[55]
CsPbBr₃(Hot-pressed)	35.07	~ 6	1.32×10^{-2}		50	5.5684×10^4	215	P	[56]
MA₃Bi₂I₉	~40	5.39	1.2×10^{-3} (out-of-plane), 2.8×10^{-3} (in plane)		120	10 620 (out-of-plane)	5.3	S	[74]

hard to obtain a bulk of big enough single crystal for flat panel imaging. But now in perovskites, this situation has been changed. Dong et al. have successfully fabricated organolead trihalide perovskite (OTP) single crystal (MAPbI₃, MA = CH₃NH₃) with long carrier diffusion lengths (> 175 μm) by low-cost solution-grown method in 2015[52]. The length of this single crystal is about 10 mm, while the thickness of that is 3 mm, as shown in Fig. 2(d). The excellent $\mu\tau$ product, high-Z elements and low-cost growth method all imply the exciting prospects of perovskite single crystals applied in X-ray detection. As expected, it was soon reported that a highly sensitive X-ray detector with a record-high $\mu\tau$ product (1.2×10^{-2} cm² V⁻¹) was made by MAPbBr₃ single crystal[16]. The sensitivity of this detector (80 μC/(Gy·cm²)) is even four times higher than the sensitivity achieved with a-Se X-ray detectors[57] and this work then intrigued many researchers[58]. Further research from this team realized simple X-ray imaging and improved the sensitivity of MAPbBr₃ single crystal X-ray detector to 2.1×10^4 μC/(Gy·cm²) by noise current suppression and applying higher working voltage[19]. Another device structure design strategy for X-ray imaging was put forward as PIN diode array, and the sensitivity of this detector based on MAPbBr₃ single crystal attained 2.36×10^4 μC/(Gy·cm²)[59].

Compared with MAPbBr₃ single crystal, X-ray detector made by MAPbI₃ single crystal is rather limited although its X-ray stopping power is stronger. Ye et al. thought it was probably because the natural geometry of MAPbI₃ single crystals is usually nonrectangular dodecahedrons, which is not as feasible as cuboid-shaped single crystals (such as MAPbBr₃) for device fabrications, especially for flat-panel array[53]. They demonstrated high-quality cuboid-MAPbI₃ single crystals by seed dissolution-regrowth (SDR) method and manufactured an X-ray detector with a favorable sensitivity. Moreover, Huang et al. used A-site cation engineering decreasing the electron-phonon coupling strength and increasing the material defect formation energy in MAPbI₃ single crystals, improved the charge collection efficiency and gained a highly efficient X-ray detector[60]. Unlike organic-inorganic hybrid perovskites, all-inorganic perovskites (such as CsPbBr₃) have attracted interest of people mainly because of their stability[61], and the replacement of organic A-site cation by metal cation (Cs⁺) also leads to better absorption efficiency for X-ray. A flexible, printable X-ray detectors based on CsPbBr₃ quantum dots (QDs) has been made[62]. Some other preliminary works making good advances have also been reported about rubidium (Rb) doped CsPbBr₃ single crystal[63] and one-dimensional CsPbI₃[64] X-ray detectors.

Because Pb²⁺ can severely damage the human brain and threaten the biological systems for the high solubility in water, the toxicity of lead halide perovskites should not be neglected[17]. Therefore, the bismuth (Bi) halide perovskites have become promising materials for X-ray detection[65]. Bi³⁺ has the same electronic configurations with Pb²⁺ and has higher atomic number (83 for Bi) that will benefit the attenuation of X-ray. A typical material of these is Cs₂AgBiBr₆ double perovskite, which was first reported in 2017 as X-ray detectors

showing an adequate low-dose X-ray detection ability (lowest detection limit: 59.7 nGy/s)[17]. This performance may be attributed to its high intrinsic resistivity and consequent low dark current. The familiar ionic migration in perovskite crystals will cause large noise and baseline drift limiting the detection and performance of X-ray, hence Yang *et al*. introduced bismuth oxybromide (BiOBr) as heteroepitaxial passivation layers to suppress ionic migration in $Cs_2AgBiBr_6$ polycrystalline wafer, decrease noises and improve sensitivity[18]. Centering on $Cs_2AgBiBr_6$ single crystal systems, multifarious approaches, such as liquid-nitrogen refrigeration[66], A-site cation engineering[67], management of crystallization temperature[68] and improved ordering of crystal structure[63], have been attempted to promote the performance of X-ray detection.

In addition to double perovskites, another low-dimensional and bismuth halide perovskite materials system has also received attention due to its unique anisotropic performance. Zhuang *et al*. showed their 2D layered perovskite-like $(NH_4)_3Bi_2I_9$ X-ray detector revealing high sensitivity of 8.2×10^3 $\mu C/(Gy \cdot cm^2)$ in the parallel direction and low detection limit of 55 nGy/s in the perpendicular direction[18]. The well performance might be ascribed to the suppression of ionic migration by the unique 2D crystal construction, reducing noise in device. Recently, X-ray detectors made by $(DMEDA)BiI_5$ (DMEDA: N,N'-dimethylethanediamine) and $(H_2MDAP)BiI_5$ (H_2MDAP = N-methyl-1,3-diaminopropanium) with one-dimensional crystal structure have been reported and achieved fair X-ray detection sensitivities[69, 70].

Fig. 2(e) shows some graphs of single crystals among part of representative perovskites discussed above, and Fig. 2(f) schematically illustrates the method of inverse temperature crystallization (ITC), which is a common and low-cost method for synthesis of perovskite single crystals[54]. In a word, perovskite single crystals have guided a new development direction for X-ray detection relying on their outstanding detecting performance.

3.3.2. Large-area fabrication of polycrystalline perovskites for X-ray detection

Actually, the first time of polycrystalline perovskites X-ray detection was before that of single crystal detection. Even so the material systems of polycrystalline perovskites X-ray detection have been hardly innovated, while the fabrication technique of large-area polycrystalline perovskite thick films for X-ray imaging has made great progress. Yakunin *et al*. firstly tried to detect X-ray and carry out X-ray imaging using a piece of polycrystalline perovskite solar cell (Fig. 2(g))[20]. In order to absorb X-ray as much as possible, they manufactured $MAPbI_3$ photovoltaic cells with thick perovskite layers (up to about 700 nm) by spin-coating method, then obtained X-ray detectors with sensitivity of 1.75 $\mu C/(Gy \cdot cm^2)$ and lastly received X-ray images by using this single-pixel detector and moving the object with an *xy* positioner[47]. In view of the low efficiency of taking X-ray images, Kim *et al*. designed a new device structure of perovskite layers especially for X-ray detection (Fig. 2(h)) and realized large-area, low-dose X-ray imaging[21]. Two interlayers of polyimide (PI)-perovskite composites were inserted by spin-casting as hole-transporting or blocking layers to reduce the dark current caused by charge injection. The high intrinsic resistivity of PI could also reduce electrical crosstalk among the pixels. The 830-μm-thick poly-

crystalline $MAPbI_3$ photoconductor layer was printed on the coated PI-$MAPbI_3$ using a doctor blade. Finally, tape-automated bonding of readout integrated circuits was performed on the X-ray detectors. The imaging area of this X-ray digital flat detector consisted of 1428×1428 pixels (10×10 cm²) with a pixel pitch of 70 μm and accomplished low-dose imaging down to 10 μGy.

In addition, two crafts have been presented for potential fabrication of large-area and high-quality polycrystalline perovskite thick films applied in X-ray imaging. The first one is a mechanical sintering process to fabricate polycrystalline $MAPbI_3$ wafers with millimeter-scale thickness and well-defined crystallinity (Fig. 2(i))[55]. It could be found that the performances of $MAPbI_3$ films were obviously elevated by their additional structure design of layers, as Fig. 2(j) shown. The second one is a hot-pressing method to fabricate thick quasi-monocrystalline $CsPbBr_3$ films (Fig. 2(k)), and a record sensitivity of 55684 $\mu C/(Gy \cdot cm^2)$ is achieved[56]. The hot-pressing method is simple and can produce thick quasi-monocrystalline $CsPbBr_3$ films with uniform orientations and large $\mu\tau$ product.

4. X-ray imaging based on perovskite detectors

4.1. Evaluation indicators of X-ray imaging

Spatial resolution is a vital performance of an X-ray imaging system. While the spatial resolution of imaging system promoted, the clearer X-ray images would be collected. The spatial resolution of the imaging system can be determined with the modulation transfer function (MTF), representing the transfer ability of input signal modulation of the spatial frequency (in line pair per millimeter; lp/mm or cycles per millimeter; cy/ mm) relative to its output[21]. An MTF value of 1 indicates the perfect detection of a given spatial frequency. To compare different detectors, it is practicable to determine the value of the spatial frequency at which the MTF drops to 0.2[75].

The slanted-edge method is frequently used to measure the curve of MTF[76]. Through processing the X-ray image of a sharp, attenuating edge device (lead foil with sharp edge, Fig. 3(a)), the edge spread function (ESF) information could be obtained. The ESF is then differentiated to get the line spread function (LSF) and the MTF similarly deduced by Fourier transformation, as the following relationship:

$$MTF(f) = F(LSF(x)) = F\left(\frac{d\,ESF(x)}{x}\right),$$

where x is the position of pixel and f is the spatial frequency. Another approach to determine MTF is very visualized, which is to take X-ray image for an X-ray resolution test chart. As shown in Fig. 3(b), this test chart made by lead film consists of many line pairs with different intervals, representing a series of spatial frequencies from low to high. The MTF of X-ray system can be estimated by observing the definition at each spatial frequency.

4.2. Common X-ray imaging systems using direct detection scenario

The most common X-ray imaging system by direct detection is flat panel X-ray imager (FPXI)[11], which is widely used in medical diagnosis, such as mammography. An FPXI consists of a large array of pixels, and each pixel has a thin film
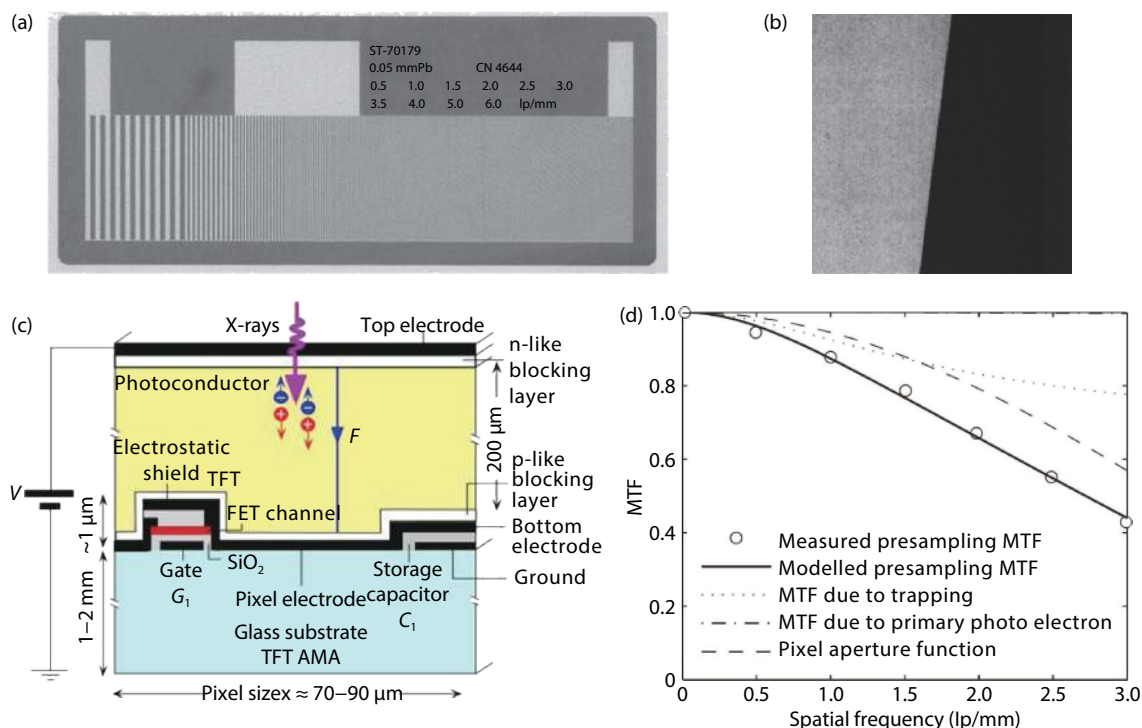
Fig. 3. (Color online) (a) X-ray image of resolution test chart. Reproduced with permission from Ref. [42]. (b) An edge X-ray image used for calculation of MTF. Reproduced with permission from Ref. [76]. (c) A simplified schematic diagram of the cross section of a single pixel with a TFT. The charges generated by the absorption of X-rays drift towards their respective electrodes. The TFT is normally off and is turned on when the gate G_1 is addressed. Reproduced with permission from Ref. [11]. (d) Idealized MTF and MTF due to trapping. Reproduced with permission from Ref. [25].

transistor (TFT) to read out the signal. This array is coated by a suitable X-ray detection material, which is then coated with electrodes on its surface to allow the application of a bias voltage. Thus, each pixel acts as an individual X-ray detector and has a biased semiconductor as illustrated in the schematic cross section of a pixel depicted in Fig. 3(c).

The spatial resolution of direct FPXI is usually much higher than that of indirect X-ray imaging system because the X-ray is not scattered but scintillation is strongly scattered in scintillators. The theoretical limit of the MTF for an FPXI is a two-dimensional sinc function in diagonal direction dominated by the pixel aperture (a)[77], as the following formula:

$$MTF(f) = sinc^2\left(\frac{af}{\sqrt{2}}\right),$$

where f is the spatial frequency. Based on the idealized situation, several factors are influencing the MTF of direct FPXI. The design of FPXI generally allows only one type of carriers (electron or hole) to be collected by TFTs[11], and the trapping of this type of carriers (such as hole in a-Se) will give rise to the degrading of MTF[78]. Kabir has created a model to investigate this phenomenon (Fig. 3(d))[25]. For some materials, the K-fluorescence reabsorption mechanism also reduces MTF, i.e., the K-edge characteristic X-ray photon is reabsorbed in a region away from the initial X-ray interaction point and hence causes blurring[79]. Besides, the lateral diffusion of carriers would spread or blur the information especially in FPXIs based on crystalline or polycrystalline semiconductors[11, 21, 80].

In current commercial direct FPXIs, the material of choice

is stabilized amorphous selenium (a-Se)[11], which is easy to integrate on large-area TFT back plate and has low dark current to reach adequate SNR under high work voltage. Fig. 4(a) demonstrates an a-Se based FPXI (AXS-2430) for mammography that has been developed and marketed by Anrad and the corresponding X-ray image of a hand taken by this FPXI. However, the practical applications of a-Se imager are still very limited, because of its low X-ray stopping power, deficient $\mu\tau$ product value, and the accompanying high operating electrical fields required to overcome its poor charge collection efficiency (Table 1)[21].

4.3. Advances of X-ray imaging based on perovskite direct-type detectors

As described above in Section 3.3, direct X-ray imaging demonstrations based on perovskite have been achieved by various means. Yakunin et al. used a MAPbI$_3$ based solar cell as a single-pixel X-ray detector, carried out scanning of the object and demonstrated a simple X-ray image of piece of leaf (Fig. 4(b))[20]. Though this imaging method was ineffective and the quality was poor, this work had certainly inspired other researchers.

Kim et al. referred the design philosophy of a-Se FPXIs, firstly manufactured a true sense of perovskite-based FPXI and successfully realized large-area X-ray imaging[21]. In this work, a demonstrative X-ray image of human hand was taken by this FPXI (Fig. 4(c)) under a low radiation dose (25 μGy) and the spatial resolution reached 3.1 lp/mm when MTF dropped to 0.2. This value was unsatisfying compared with that of a-Se FPXI (7.1 lp/mm at MTF = 0.2), and they speculated it to MAPbI$_3$ crystallites of 20 to 100 μm size that are lar-
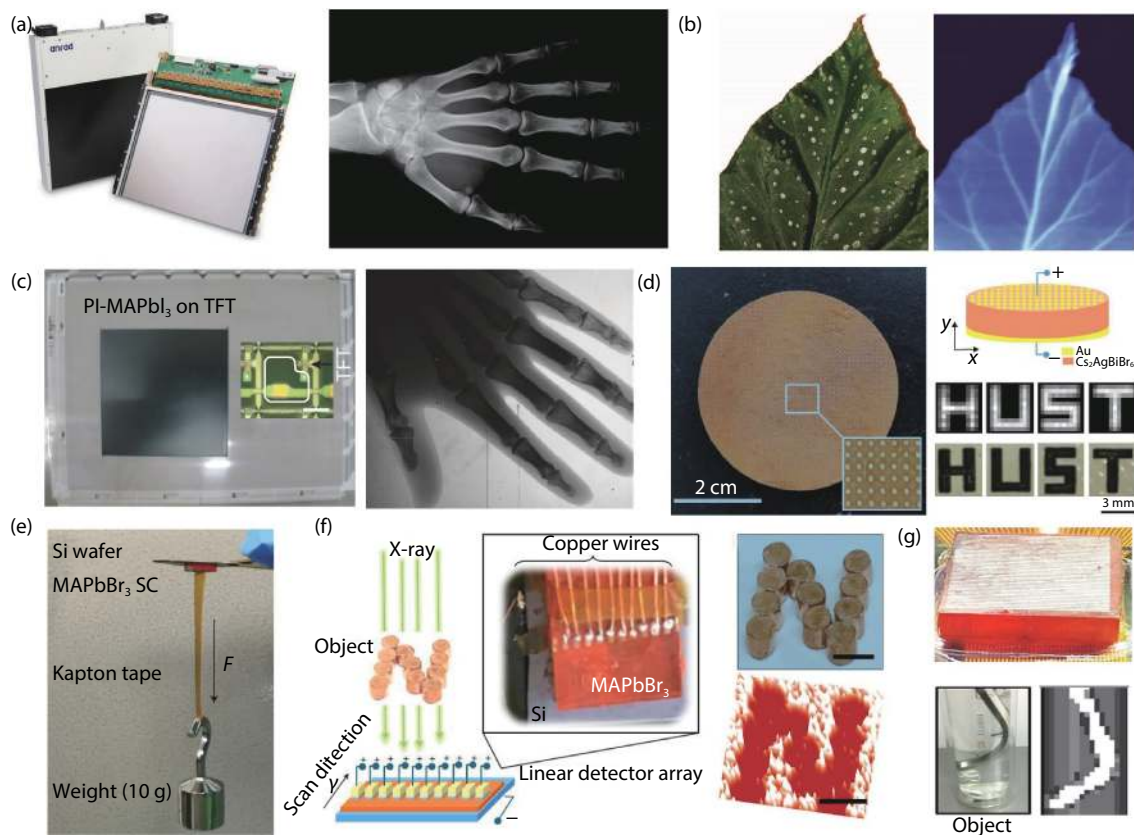
Fig. 4. (Color online) (a) Left: Anrad's mammographic FPXI (AXS-2430) is used in mammography markets. The field of view is 24×30 cm^2 and the FPXI have a pixel pitch of 85 μm. Right: an X-ray image of a hand from AXS-2430. Reproduced with permission from Ref. [11]. (b) Photograph (left) and corresponding X-ray image (right) of a leaf, obtained with the photoconductor in Ref. [20]. Reproduced with permission from Ref. [20]. (c) Left: image of spin-cast PI-MAPbI$_3$ on an a-Si:H TFT backplane. The inset in the left shows a single-pixel structure of TFT (scale bar 30 μm). Right: A hand X-ray image obtained from this MAPbI$_3$ FPXI. Reproduced with permission from Ref. [21]. (d) Left: The fabricated multi-pixel wafer-based Cs$_2$AgBiBr$_6$ polycrystalline detector. Right top: schematic illustration of the imaging process. Right bottom: X-ray image and optical image of 'HUST' symbol. Reproduced with permission from Ref. [18]. (e) Photograph of Si-integrated MAPbBr$_3$ single crystal with a 10 g weight attached to the MAPbBr$_3$ crystal. Reproduced with permission from Ref. [19]. (f) Left: schematic illustration of X-ray imaging with Si-integrated MAPbBr$_3$ single crystal detectors. Right: photo (top) and X-ray image (bottom) of an 'N' copper logo. Reproduced with permission from Ref. [19]. (g) Top: photo of the PIN array. Bottom: object photo (left) and X-ray image (right) for 100 keV energy. Reproduced with permission from Ref. [59].

ger than a pixel size and can overlap adjacent pixels, leading to charge sharing among pixels.

In addition, Yang *et al.* fabricated a large-area (5 cm of diameter) Cs$_2$AgBiBr$_6$ polycrystalline wafer by the isostatic-pressing process, then Au electrodes array was thermally evaporated on the wafer to accomplish preliminary X-ray imaging (6×6 array, Fig. 4(d))[18]. In this work, MTF was measured as 4.9 lp/mm when MTF value was equal to 0.2 by point-scanning method without read out integrated circuit (ROIC).

On the other hand, X-ray imaging attempts by means of perovskite single crystals have made some good advances as well. Wei *et al.* reported a low-temperature solution-processed molecular bonding method with the assistance of brominated APTES molecules[19]. They firmly integrated MAPbBr$_3$ single crystal with Si wafer by utilizing this method (Fig. 4(e)), which made the perovskite single-crystal FPXI possible. Then the X-ray image of 'N' copper logo was taken by this integrated Si-perovskite single crystal on which ten pixel electrodes (linear array with pixel size of 200 μm and a pitch of 400 μm) were deposited (Fig. 4(f)). During the imaging process, the object was scanning by the linear detection array. Inspired by this design, Wang *et al.* decided to fabricate PIN diodes array on MAPbBr$_3$ single crystal, attaining X-ray images

under different X-ray photon energies (Fig. 4(g))[59].

5. Summary and outlook

From this review, it could be seen that direct-type perovskite X-ray detection and imaging have revealed vast potentials for future applications. Compared to a-Se, perovskite semiconductor has many significant advantages including strong X-ray stopping power, remarkable carrier transport ability, high intrinsic sensitivity, low detection limit and inexpensive solution-processed fabrication. However, there still exist some issues to be addressed to facilitate the commercialization.

Firstly, more physical insights are encouraged to understand and guide the material optimization and device design in order to fulfill high sensitivity and low noise. For example, the narrower bandgap leads to smaller $W_{\pm}$, and higher intrinsic X-ray sensitivity, while the broader bandgap material usually gives larger resistance and therefore lower noise. Hence, an optimal bandgap needs to be selected for the sake of balancing sensitivity and noise, after all, the X-ray imaging requires adequate SNR with as low dose as possible. We might overemphasized on high sensitivity while ignored the noise reduction, particularly those devices with large trap-assisted pho-

toconductive gains, they might not be so useful for practical applications, because the noises are also increased because of the traps, and ultimately the SNRs are sacrificed. Secondly, it is important to understand and identify the factors that limit the special resolution of the X-ray imaging. It was found that perovskite-based FPXI had much lower spatial resolution than that of a-Se[21], but the reason was not clear yet. Trapping and lateral diffusion of carriers in polycrystalline perovskite film are inferred as probable origins. The promotion of spatial resolution in perovskite FPXI is an important aim in next stage. Thirdly, low-cost method to fabricate large-area high-quality perovskite thick film (~ 1 mm) should be further explored. Some of the previous methods required high temperature, which not only increased the processing difficulty but also made them questionable when integrating with α-Si TFT back panel[19]. Fourthly, new perovskite derivatives are worthy to be explored, such as double perovskites and low-dimension perovskites[17, 18], which are able to provide new possibilities for the performance improvement for X-ray detection and imaging. In addition, the radiation hardness of perovskite X-ray detector is also an important factor. There are a few very encouraging results on perovskite radiation stability reported[49]. However, more data related with radiation hardness are certainly encouraged, and the testing methods need to be standardized.

In conclusion, more efforts should be contributed to the theorical understanding, fabrication methods and attempting of new materials for perovskite direct X-ray detectors. We believe that the perovskites will emerge as a splendid X-ray detecting material and hold a bright future for practical X-ray imaging applications.

References

[1] Spahn M. X-ray detectors in medical imaging. Nucl Instrum Methods Phys Res A, 2013, 731, 57

[2] Van Eijk C W. Inorganic scintillators in medical imaging. Phys Med Biol, 2002, 47, R85

[3] Duan X, Cheng J, Zhang L, et al. X-ray cargo container inspection system with few-view projection imaging. Nucl Instrum Methods Phys Res A, 2009, 598, 439

[4] Haff R P, Toyofuku N. X-ray detection of defects and contaminants in the food industry. Sens Instrum Food Quality Safety, 2008, 2, 262

[5] Chapman H N, Fromme P, Barty A, et al. Femtosecond X-ray protein nanocrystallography. Nature, 2011, 470, 73

[6] Nielsen J A, McMorrow D. Elements of modern X-ray physics. Wiley, 2011

[7] Moses W W. Scintillator requirements for medical imaging. LBNL Publications, 1999

[8] Lin E C. Radiation risk from medical imaging. In: Mayo Clinic Proceedings. Elsevier, 2010, 1142

[9] Knoll G F. Radiation detection and measurement. John Wiley & Sons, 2010

[10] Rowlands J A. Medical imaging: Material change for X-ray detectors. Nature, 2017, 550, 47

[11] Kasap S, Frey J B, Belev G, et al. Amorphous and polycrystalline photoconductors for direct conversion flat panel X-ray image sensors. Sensors, 2011, 11, 5112

[12] Zheng X, Chen B, Dai J, et al. Defect passivation in hybrid perovskite solar cells using quaternary ammonium halide anions and cations. Nat Energy, 2017, 2, 17102

[13] Xiao Z, Kerner R A, Zhao L, et al. Efficient perovskite light-emitting diodes featuring nanometre-sized crystallites. Nat Photonics, 2017, 11, 108

[14] Saliba M, Wood S M, Patel J B, et al. Structured organic–inorganic perovskite toward a distributed feedback laser. Adv Mater, 2016, 28, 923

[15] Dou L, Yang Y M, You J, et al. Solution-processed hybrid perovskite photodetectors with high detectivity. Nat Commun, 2014, 5, 5404

[16] Wei H, Fang Y, Mulligan P, et al. Sensitive X-ray detectors made of methylammonium lead tribromide perovskite single crystals. Nat Photonics, 2016, 10, 333

[17] Pan W, Wu H, Luo J, et al. $Cs_2AgBiBr_6$ single-crystal X-ray detectors with a low detection limit. Nat Photonics, 2017, 11, 726

[18] Zhuang R, Wang X, Ma W, et al. Highly sensitive X-ray detector made of layered perovskite-like $(NH_4)_3Bi_2I_9$ single crystal with anisotropic response. Nat Photonics, 2019, 13, 602

[19] Wei W, Zhang Y, Xu Q, et al. Monolithic integration of hybrid perovskite single crystals with heterogenous substrate for highly sensitive X-ray imaging. Nat Photonics, 2017, 11, 315

[20] Yakunin S, Sytnyk M, Kriegner D, et al. Detection of X-ray photons by solution-processed lead halide perovskites. Nat Photonics, 2015, 9, 444

[21] Kim Y C, Kim K H, Son D Y, et al. Printable organometallic perovskite enables large-area, low-dose X-ray imaging. Nature, 2017, 550, 87

[22] Martin J E. Physics for radiation protection: a handbook. John Wiley & Sons, 2006

[23] Wei H, Huang J. Halide lead perovskites for ionizing radiation detection. Nat Commun, 2019, 10, 1066

[24] Devanathan R, Corrales L R, Gao F, et al. Signal variance in gamma-ray detectors—A review. Nucl Instrum Methods Phys Res A, 2006, 565, 637

[25] Kabir M. Effects of charge carrier trapping on polycrystalline PbO X-ray imaging detectors. J Appl Phys, 2008, 104, 074506

[26] Klein C A. Bandgap dependence and related features of radiation ionization energies in semiconductors. J Appl Phys, 1968, 39, 2029

[27] Alig R, Bloom S. Electron-hole-pair creation energies in semiconductors. Phys Rev Lett, 1975, 35, 1522

[28] van Heerden P J. The crystalcounter. Noord-Holl Uitg Mij, 1945

[29] McKay K G. A germanium counter. Phys Rev, 1949, 76, 1537

[30] Guerra M, Manso M, Longelin S, et al. Performance of three different Si X-ray detectors for portable XRF spectrometers in cultural heritage applications. J Instrum, 2012, 7, C10004

[31] Owens A, Peacock A. Compound semiconductor radiation detectors. Nucl Instrum Methods Phys Res A, 2004, 531, 18

[32] Del Sordo S, Abbene L, Caroli E, et al. Progress in the development of CdTe and CdZnTe semiconductor radiation detectors for astrophysical and medical applications. Sensors, 2009, 9, 3491

[33] Luke P, Rossington C, Wesela M. Low energy X-ray response of Ge detectors with amorphous Ge entrance contacts. IEEE Trans Nucl Sci, 1994, 41, 1074

[34] Szeles C. CdZnTe and CdTe materials for X-ray and gamma ray radiation detector applications. Phys Status Solidi B, 2004, 241, 783

[35] Zentai G, Schieber M, Partain L, et al. Large area mercuric iodide and lead iodide X-ray detectors for medical and non-destructive industrial imaging. J Cryst Growth, 2005, 275, e1327

[36] Schieber M M, Zuck A, Melekhov L, et al. High-flux X-ray response of composite mercuric iodide detectors. In: Hard X-Ray, Gamma-Ray, and Neutron Detector Physics. International Society for Optics and Photonics, 1999, 296

[37] Street R, Ready S, Van Schuylenbergh K, et al. Comparison of PbI_2 and HgI_2 for direct detection active matrix X-ray image sensors. J Appl Phys, 2002, 91, 3345

[38] Schieber M, Hermon H, Zuck A, et al. Thick films of X-ray polycrystalline mercuric iodide detectors. J Cryst Growth, 2001, 225, 118

[39] Zentai G, Partain L D, Pavlyuchkova R, et al. Mercuric iodide and lead iodide X-ray detectors for radiographic and fluoroscopic medical imaging In: Medical Imaging 2003: Physics of Medical Imaging. International Society for Optics and Photonics, 2003, 77

[40] Yun M S, Cho S H, Lee R, et al. Investigation of PbI$_2$ film fabricated by a new sedimentation method as an X-ray conversion material. Jpn J Appl Phys, 2010, 49, 041801

[41] Shah K, Street R, Dmitriyev Y, et al. X-ray imaging with PbI$_2$-based a-Si: H flat panel detectors. Nucl Instrum Methods Phys Res A, 2001, 458, 140

[42] Simon M, Ford R, Franklin A, et al. Analysis of lead oxide (PbO) layers for direct conversion X-ray detection. IEEE Symposium Conference Record Nuclear Science, 2004, 4268

[43] Destefano N, Mulato M. Influence of multi-depositions on the final properties of thermally evaporated TlBr films. Nucl Instrum Methods Phys Res A, 2010, 624, 114

[44] Hitomi K, Kikuchi Y, Shoji T, et al. Improvement of energy resolutions in TlBr detectors. Nucl Instrum Methods Phys Res A, 2009, 607, 112

[45] Brenner T M, Egger D A, Kronik L, et al. Hybrid organic–inorganic perovskites: low-cost semiconductors with intriguing charge-transport properties. Nat Rev Mater, 2016, 1, 15007

[46] de Arquer F P G, Armin A, Meredith P, et al. Solution-processed semiconductors for next-generation photodetectors. Nat Rev Mater, 2017, 2, 16100

[47] Kasap S. Low-cost X-ray detectors. Nat Photonics, 2015, 9, 420

[48] Lang F, Nickel N H, Bundesmann J, et al. Radiation hardness and self-healing of perovskite solar cells. Adv Mater, 2016, 28, 8726

[49] Yang S, Xu Z, Xue S, et al. Organohalide lead perovskites: more stable than glass under gamma-ray radiation. Adv Mater, 2019, 31, 1805547

[50] Huang J, Yuan Y, Shao Y, et al. Understanding the physical properties of hybrid perovskites for photovoltaic applications. Nat Rev Mater, 2017, 2, 17042

[51] Lang F, Shargaieva O, Brus V V, et al. Influence of radiation on the properties and the stability of hybrid perovskites. Adv Mater, 2018, 30, 1702905

[52] Dong Q, Fang Y, Shao Y, et al. Electron–hole diffusion lengths > 175 μm in solution-grown CH$_3$NH$_3$PbI$_3$ single crystals. Science, 2015, 347, 967

[53] Ye F, Lin H, Wu H, et al. High-quality cuboid CH$_3$NH$_3$PbI$_3$ single crystals for high performance X-ray and photon detectors. Adv Funct Mater, 2019, 29, 1806984

[54] Saidaminov M I, Abdelhady A L, Murali B, et al. High-quality bulk hybrid perovskite single crystals within minutes by inverse temperature crystallization. Nat Commun, 2015, 6, 1

[55] Shrestha S, Fischer R, Matt G J, et al. High-performance direct conversion X-ray detectors based on sintered hybrid lead triiodide perovskite wafers. Nat Photonics, 2017, 11, 436

[56] Pan W, Yang B, Niu G, et al. Hot-pressed CsPbBr$_3$ quasi-monocrystalline film for sensitive direct X-ray detection. Adv Mater, 2019, 31, 1904405

[57] Kasap S. X-ray sensitivity of photoconductors: application to stabilized a-Se. J Phys D, 2000, 33, 2853

[58] Heiss W, Brabec C. X-ray imaging: Perovskites target X-ray detection. Nat Photonics, 2016, 10, 288

[59] Wang X, Zhao D, Qiu Y, et al. PIN diodes array made of perovskite single crystal for X-ray imaging. Phys Status Solidi RRL, 2018, 12, 1800380

[60] Huang Y, Qiao L, Jiang Y, et al. A-site cation engineering for highly efficient MAPbI$_3$ single-crystal X-ray detector. Angew Chem Int Ed, 2019, 58, 17834

[61] Eperon G E, Paterno G M, Sutton R J, et al. Inorganic caesium lead iodide perovskite solar cells. J Mater Chem A, 2015, 3, 19688

[62] Liu J, Shabbir B, Wang C, et al. Flexible, printable soft-X-ray detectors based on all-inorganic perovskite quantum dots. Adv Mater, 2019, 31(30), 1901644

[63] Yuan W, Niu G, Xian Y, et al. In situ regulating the order–disorder phase transition in Cs$_2$AgBiBr$_6$ single crystal toward the application in an X-ray detector. Adv Funct Mater, 2019, 29, 1900234

[64] Zhang B, Liu X, Xiao B, et al. High performance X-ray detection based on one-dimensional inorganic halide perovskite CsPbI$_3$. J Phys Chem Lett, 2020, 11, 43

[65] Wu C, Zhang Q, Liu G, et al. From Pb to Bi: a promising family of Pb-free optoelectronic materials and devices. Adv Energy Mater, 2019, 10, 1902496

[66] Steele J A, Pan W, Martin C, et al. Photophysical pathways in highly sensitive Cs$_2$AgBiBr$_6$ double-perovskite single-crystal X-ray detectors. Adv Mater, 2018, 30, 1804450

[67] Xu Z, Liu X, Li Y, et al. Exploring lead-free hybrid double perovskite crystals of (BA)$_2$CsAgBiBr$_7$ with large mobility-lifetime product toward X-ray detection. Angew Chem Int Ed, 2019, 58, 15757

[68] Yin L, Wu H, Pan W, et al. Controlled cooling for synthesis of Cs$_2$AgBiBr$_6$ single crystals and its application for X-ray detection. Adv Opt Mater, 2019, 7, 1900491

[69] Yao L, Niu G, Yin L, et al. Bismuth halide perovskite derivatives for direct X-ray detection. J Mater Chem C, 2020, 8, 1239

[70] Tao K, Li Y, Ji C, et al. A lead-free hybrid iodide with quantitative response to X-ray radiation. Chem Mater, 2019, 31, 5927

[71] Rikner G, Grusell E. Effects of radiation damage on p-type silicon detectors. Phys Med Biol, 1983, 28, 1261

[72] Bellazzini R, Spandre G, Brez A, et al. Chromatic X-ray imaging with a fine pitch CdTe sensor coupled to a large area photon counting pixel ASIC. J Instrum, 2013, 8, C02028

[73] Ivanov Y M, Kanevsky V, Dvoryankin V, et al. The possibilities of using semi-insulating CdTe crystals as detecting material for X-ray imaging radiography. Phys Status Solidi C, 2003, 0(3), 840

[74] Zheng X, Zhao W, Wang P, et al. Ultrasensitive and stable X-ray detection using zero-dimensional lead-free perovskites. J Energy Chem, 2020, 49, 299

[75] Büchele P, Richter M, Tedde S F, et al. X-ray imaging with scintillator-sensitized hybrid organic photodetectors. Nat Photonics, 2015, 9, 843

[76] Samei E, Flynn M J, Reimann D A. A method for measuring the presampled MTF of digital radiographic systems using an edge test device. Med Phys, 1998, 25, 102

[77] Hoheisel M, Batz L, Mertelmeier T, et al. Modulation transfer function of a selenium-based digital mammography system. IEEE Trans Nucl Sci, 2006, 53, 1118

[78] Kabir M Z, Kasap S. Modulation transfer function of photoconductive X-ray image detectors: effects of charge carrier trapping. J Phys D, 2003, 36, 2352

[79] Hunter D M, Belev G, Kasap S, et al. Measured and calculated K-fluorescence effects on the MTF of an amorphous-selenium based CCD X-ray detector. Med Phys, 2012, 39, 608

[80] Kozorezov A G, Wigmore J, Owens A, et al. The effect of carrier diffusion on the characteristics of semiconductor imaging arrays. Nucl Instrum Methods Phys Res A, 2004, 531, 52